Investigation of the sideband effect for the LCL-type grid-connected inverter with high LCL resonance frequency

Yang, Dongsheng; Wang, Xiongfei; Blaabjerg, Frede

Published in:
Proceedings of 2017 IEEE Energy Conversion Congress and Exposition (ECCE)

DOI (link to publication from Publisher):
10.1109/ECCE.2017.8096932

Publication date:
2017

Document Version
Accepted author manuscript, peer reviewed version

Investigation of the Sideband Effect for the LCL-type Grid-connected Inverter with High LCL Resonance Frequency

Dongsheng Yang, Xiongfei Wang, Frede Blaabjerg
Department of Energy Technology, Aalborg University.
Pontoppidanstraede 101, Aalborg, 9220, Denmark
doy@et.aau.dk, xwa@et.aau.dk, fbl@et.aau.dk

***Abstract*—The LCL-type grid connected inverter has been widely used as the intelligent power interface between the distributed generation unit and the power grid. To reduce the cost and volume of the filter, it is desirable to design the LCL filter with higher resonance frequency provided that the quality of injected grid current is not compromised. Actually, it is the typical case for the T-type or NPC three-level inverter to design its LCL resonance frequency close to half of the switching frequency. In this case, however, the sideband effect of SPWM modulation can impose a significant impact on the system stability, and the traditional ZOH model is inadequate to describe the dynamic behavior of the digital SPWM modulator. In this paper, by extending the multi-frequency model to AC system, the stability of the grid-connected inverter is examed with the consideration of sideband effect. An interesting discovery in this paper is that the influence of grid voltage on the system stability can be successfully predicted, which provides a useful tool to study the stability of inverter in presence of large grid voltage disturbances. Experimental results from a down-scaled three-phase inverter confirm the effectiveness of stability analysis.**

Keywords—grid-connected inverters* ; *LCL filter* ; *sideband harmonics, multi-frequency model

I. INTRODUCTION

Driven by urgent demands of clean and sustainable energy, the renewable-energy-based distributed generation (DG) has been developed rapidly in the past decades [1]. Featuring full control flexibility and high efficiency, the LCL-filtered voltage source inverter (VSI) is widely used as the interface between the renewable energy source and the power grid. The dynamic coupling of grid connected inverters through the grid impedance tends to bring in a wide frequency range of resonances and harmonic instability, challenging stable operations of modern power systems [2]. To effectively address this issue, the impedance-based approach has been recently developed in [3], [4], which not only provides an intuitive insight of the interactions among the VSIs and the grid but also enables to reshape inverter control output impedance for stabilizing the power system [5]-[6].

The impedance model developed for the stability analysis is usually based on the averaged small-signal model, where the sideband harmonics generated by the digital modulator have been neglected by small ripple approximation [7]. However, this is not always true. By employing the high-order filters, such as LCL filter, LLCL filter, LTCL filter, etc., the resonance frequency of filters can be designed to be near Nyquist frequency for a cost-effective design without compromising the quality of the injected grid current [8]-[9]. In this case, the sideband components may impose a significant impact on the dynamics of the inverters and the sideband harmonic resonance may be triggered.

Common practice in modeling the digital SPWM modulator is to represent it by Zero-Order Holder (ZOH), but ZOH only takes the sampling and hold procedure into consideration. In fact, the SPWM modulation will generate abound of sideband components, especially when the PWM reference contains small-signal perturbations besides the fundamental wave. Therefore, ZOH model may lose much of the essential dynamics digital SPWM modulator. In order to fully describe the high-nonlinearity of PWM modulation, multi-frequency model has been developed in the dc system both for the analog control [10] and digital control [11]. Yet, both the multi-frequency model and the impedance matrix are established at the dc steady-state operating point, which is not readily used for the paralleled inverters, due to the time-varying operating point with the sinusoidal fundamental waveform. In [12], multiple-frequency input admittance is derived to assess the passivity of the inverter above the Nyquist frequency. It only considers the sideband harmonics generated by sampling processes, while neglecting the sideband harmonics generated by the sinusoidal PWM modulator. In this paper, by investigating the relationship between the sideband and perturbation frequency components, the multi-frequency model is extended to the AC system. With this model, the influence of grid voltage on the system stability can be successfully predicted, which provides a useful tool to study the stability of inverters when the grid is experienced with large voltage disturbances.

II. MULTI-FREQUENCY MODEL OF THE DIGITAL SPWM MODULATOR

Compared with the harmonic spectrum of PWM modulation in DC system, the harmonic spectrum of sinusoidal PWM modulation in AC system is much more

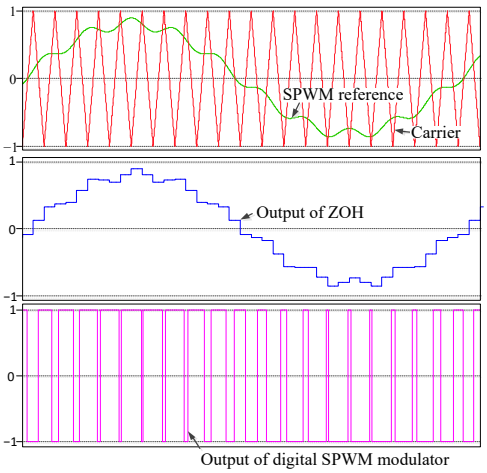

Fig. 1 Outputs of ZOH and the digital sinusoidal PWM modulator

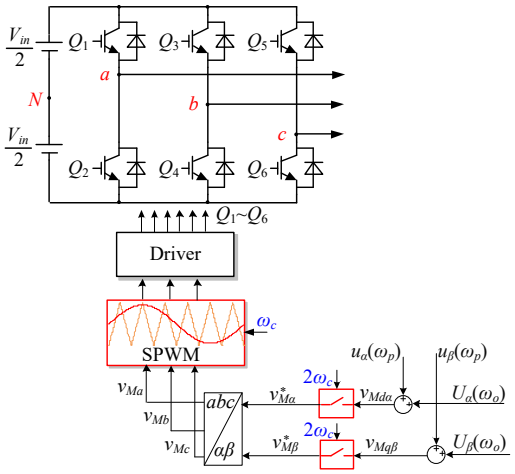

Fig. 2 Digital sinusoidal PWM modulator with small-signal perturbation

complicated when the reference modulating waveform contains both the fundamental and perturbation components. Moreover, when the digital control is employed, the sampling and hold (S&H) procedure also introduces sideband components [11]. Therefore, when the sampling frequency is different from the switching (carrier-) frequency, the output of the digital sinusoidal PWM modulator will contain multiple sideband harmonics. Common practice in modeling the digital sinusoidal PWM modulator is to use the Zero-Order Hold (ZOH), which can be expressed by:

$$G_h(s) = \frac{1 - e^{-T_s s}}{T_s s} \tag{1}$$

where T_s is the sampling frequency.

However, the ZOH only takes the S&H procedure into consideration, which neglects the inherent nonlinearity of the sinusoidal PWM. As shown in Fig.1, an obvious mismatch can be observed between the output waveform of ZOH and a digital sinusoidal PWM modulator. Hence, such a ZOH model is inadequate to capture the sideband component of the digital sinusoidal PWM modulator.

The harmonics in the output of the digital sinusoidal PWM modulator can be divided into two types. The first type is the static harmonics, which are constant and not affected by the perturbations, while the other is the dynamic harmonics which are changed along with perturbations. As for the static harmonics, the analytical methods have been well developed based on the double Fourier analysis [13]. However, the analysis of dynamic harmonics, which may have a significant influence on system dynamic performance and stability, are usually overlooked.

To fully capture the characteristics of dynamic harmonics, a small-signal perturbation is intentionally injected into the PWM reference waveform under $\alpha\beta$ frame, as shown in Fig. 2. Then by calculating the spectra of inverter output voltage analytically, the frequency response of the digital sinusoidal PWM modulator can be derived at both the perturbation frequency and sideband frequency based on the harmonic balance principle [14].

To simplify the analysis, all the variables are transferred to the $\alpha\beta$ frame and represented by the complex space vector. Thus, the three-phase system can be represented by single-phase system, provided that the three-phase components are balanced. As shown in Fig. 2, the angular frequency of the carrier waveform is ω_c, and the sampling frequency is ω_s. In this work, the double update of the duty cycle is adopted, i.e. the digital control system is sampled and updated twice for each switching cycle, $\omega_s = 2\omega_c$. A small-signal perturbation component $\boldsymbol{u}_{\alpha\beta}$ at the frequency ω_p is intentionally added to the fundamental wave $\boldsymbol{U}_{\alpha\beta}$. The complex vectors of $\boldsymbol{u}_{\alpha\beta}$ and $\boldsymbol{U}_{\alpha\beta}$ in the frequency domain can be represented by:

$$\boldsymbol{u}_{\alpha\beta}(\omega) = u_\alpha(\omega) + j u_\beta(\omega) = M_p 2\pi \cdot e^{j\theta_p} \cdot \delta(\omega - \omega_p) \tag{2}$$

$$\boldsymbol{U}_{\alpha\beta}(\omega) = U_\alpha(\omega) + j U_\beta(\omega) = M_0 2\pi \cdot e^{j\theta_0} \cdot \delta(\omega - \omega_0) \tag{3}$$

where M_p and M_0 are the modulation ratios of $u_{\alpha\beta}$ and $U_{\alpha\beta}$, respectively; θ_p and θ_0 are initial phase angle of $\boldsymbol{u}_{\alpha\beta}$ and $\boldsymbol{U}_{\alpha\beta}$, respectively. Under small-signal assumption, we have $M_p \ll M_0$.

Using one-dimensional spectral analysis method proposed in [15], the harmonic spectrum of inverter output voltages in the $\alpha\beta$ frame can be derived as (4) shown on the top of next page, where θ_c, is the initial phase angle of the carrier, and m, n_0 and n_p are the index variables of the carrier, fundamental wave and small-signal perturbation, respectively. J_n is the n order of first kind Bessel function, which is expressed as

$$J_n(x) = \frac{1}{2\pi}\int_0^{2\pi} \cos(n\tau - x\sin\tau) d\tau \tag{5}$$

According to the Fourier analysis given in (4), the harmonic spectra of the inverter output voltage in the three different cases are shown in Fig. 3. First, when the PWM reference contains only the sinusoidal fundamental waveform, as shown in Fig. 3(a), the dominant harmonics are around

$$v_{inv\_\alpha\beta}(\omega)=u_{inv\_\alpha}(\omega)+ju_{inv\_\beta}(\omega)$$

$$=\sum_{m=-\infty}^{\infty}\sum_{n_0=-\infty}^{\infty}\sum_{n_p=-\infty}^{\infty}\left\{\begin{array}{l}\left(\frac{2}{3}\left(1-2\cos\left(\frac{2n_0+2n_p+1}{3}\pi\right)\right)\cdot\frac{4}{m+n_0\frac{\omega_0}{\omega_c}+n_p\frac{\omega_p}{\omega_c}}\sin\left(\left(m+n_0+n_p\right)\frac{\pi}{2}\right)\right.\\ \left.\cdot J_{n_0}\left(\frac{\pi}{2}\left(m+n_0\frac{\omega_0}{\omega_c}+n_p\frac{\omega_p}{\omega_c}\right)M_0\right)\cdot J_{n_p}\left(\frac{\pi}{2}\left(m+n_0\frac{\omega_0}{\omega_c}+n_p\frac{\omega_p}{\omega_c}\right)M_p\right)\cdot e^{j\left(n_0\theta_0+n_p\theta_p+m\theta_c\right)}\cdot\delta\left(\omega-m\omega_c-n_0\omega_0-n_p\omega_p\right)\right)\\ +\left(\frac{2}{3}\left(1-2\cos\left(\frac{2n_0+2n_p-1}{3}\pi\right)\right)\cdot\frac{4}{m+n_0\frac{\omega_0}{\omega_c}+n_p\frac{\omega_p}{\omega_c}}\sin\left(\left(m+n_0+n_p\right)\frac{\pi}{2}\right)\right.\\ \left.\cdot J_{n_0}\left(\frac{\pi}{2}\left(m+n_0\frac{\omega_0}{\omega_c}+n_p\frac{\omega_p}{\omega_c}\right)M_0\right)\cdot J_{n_p}\left(\frac{\pi}{2}\left(m+n_0\frac{\omega_0}{\omega_c}+n_p\frac{\omega_p}{\omega_c}\right)M_p\right)\cdot e^{-j\left(n_0\theta_0+n_p\theta_p+m\theta_c\right)}\cdot\delta\left(\omega+m\omega_c+n_0\omega_0+n_p\omega_p\right)\right)\end{array}\right\} \quad (4)$$

$0.5\omega_s$ and ω_s, which are static harmonics. Secondly, when the PWM reference contains only the small-signal perturbation ω_p, as shown in Fig. 3(b), the resulting sideband harmonic is at the frequency $\omega_s-\omega_p$, which is the dynamic harmonic. Lastly,

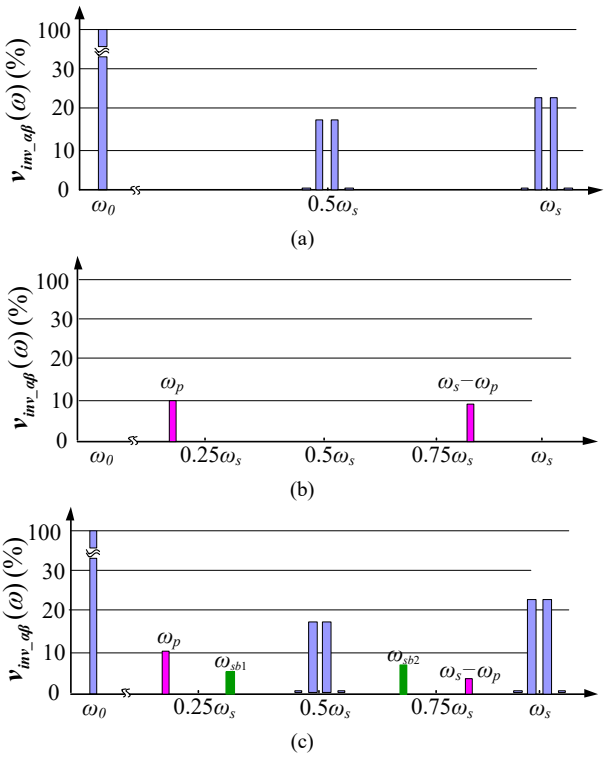

Fig. 3 Harmonic spectra of the inverter output voltage with PWM reference containing (a) only fundamental wave, (b) only small-signal perturbation, (c) both the fundamental wave and small signal perturbation.

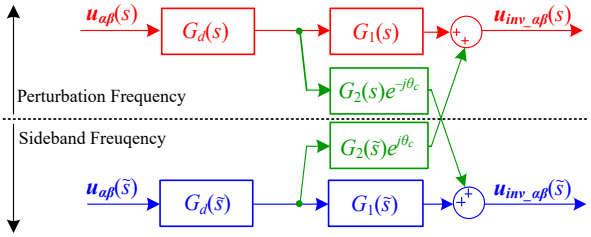

Fig. 4 Multi-frequency model for the digital sinusoidal PWM modulator

when the PWM reference contains both the sinusoidal fundamental wave and the small-signal perturbation, as shown in Fig. 3(c), the static harmonics are the same with that in Fig. 3(a). However, the dynamic harmonics are different from that in Fig. 3(b). New sideband harmonic components are generated at the relatively low-frequency range, of which the frequencies ω_{sb1} and ω_{sb2} are also affected by the phase sequence of the perturbation.

In this paper, it is assumed that the dynamic harmonic components beyond the Nyquist frequency $0.5\omega_s$ are well attenuated by the power filter and the anti-aliasing filter. Only the lowest sideband harmonic component at ω_{sb1} is taken into account when modeling the digital sinusoidal PWM modulator.

According to (2) and (4), the relationship between the According to (2) and (4), the relationship between the perturbation and the corresponding dominant sideband components is derived based on the harmonic balance principle, which is illustrated by the multi-frequency model shown in Fig. 4. The dynamics of two frequency components, i.e., the perturbation frequency component and the sideband frequency component, have been taken into consideration. As for the positive sequence perturbation, i.e., $\omega_p\geq 0$, the dominant sideband component is $\omega_{sb1}=\omega_p+\omega_0-\omega_c$. If $s=j\omega_p$ is used as the Laplace variable at the perturbation frequency, $\tilde{s}=s+j\left(\omega_0-\omega_c\right)$ is thereby used as Laplace variable at the sideband frequency. As for the negative sequence perturbation, i.e., $\omega_p<0$, the dominated sideband component is $\omega_{sb1}=\omega_p+\omega_0+\omega_c$, so $\tilde{s}=s+j(\omega_0+\omega_c)$ is thereby used as Laplace variable of the sideband frequency.

In Fig. 4, $G_d(s)$ represents the delay caused by the sampling and hold, which is given by

$$G_d(s)=e^{-0.5sT_s} \quad (6)$$

The transfer function $G_1(s)$ is the representation of the sampler and modulator of the single frequency, which is expressed as:

$$G_1(s) = J_0\left(\frac{\pi}{2}\frac{|s|}{\omega_c}\mathrm{M}_0\right) \tag{7}$$

The transfer function $G_2(s)$ is used to denote the dynamic coupling between the perturbation frequency and the sideband frequency components. Since the dominant side-band frequency is different for the positive-sequence and negative-sequence component of $\boldsymbol{u_{\alpha\beta}(\omega_p)}$, the expression of $G_2(s)$ is also different depending on the sequence of $\boldsymbol{u_{\alpha\beta}(\omega_p)}$, which can be expressed as:

$$G_2(s) = \begin{cases} -J_1\left(\frac{\pi}{2}\left(1-\frac{|s|+\omega_0}{\omega_c}\right)\mathrm{M}_0\right)\left(\omega_p \geq 0\right) \\ -J_1\left(\frac{\pi}{2}\left(1+\frac{-|s|+\omega_0}{\omega_c}\right)\mathrm{M}_0\right)\left(\omega_p < 0\right) \end{cases} \tag{8}$$

It is worth noting that this multi-frequency model can be readily transformed from the $\alpha\beta$-frame to the dq-frame, simply by replacing the Laplace variables s and $\tilde{s}$ with $s+j\omega_0$ and $\tilde{s}+j\omega_0$, respectively, according to the frequency translation between the $\alpha\beta$ frame and dq frame [2].

III. Passivity-Based Stability Analysis with Consideration of Sideband Effect

In order to investigate the impact of the sideband components on the system stability, the passivity-based stability analysis is used in this paper to provide a more intuitive insight [4].

The control scheme of the three-phase grid-connected inverter under study is shown in Fig. 5. A three-phase voltage-source inverter (VSI) consisting of $Q_1 \sim Q_6$ is connected to the grid through an LCL filter. L_1 is the inverter-side inductor, C is the filter capacitor, and L_2 is the grid-side inductor. V_{in} is the input dc voltage, and v_{pcc_a}, v_{pcc_b} and v_{pcc_c} are the three-phase grid voltages at the point of common coupling (PCC). In this paper, the inverter-side currents are controlled under the $\alpha\beta$ frame, and the capacitor voltage v_C is fed-forward to actively

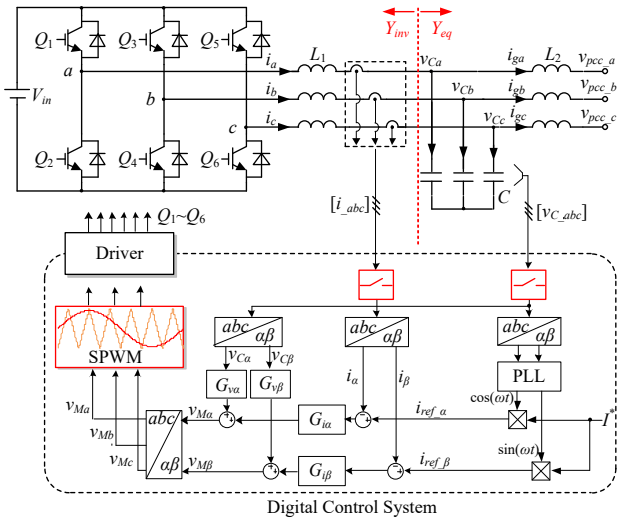

Fig. 5 Control scheme of the three-phase grid-connected inverter

damp resonance peak of the LCL filter. G_i is the PR current regulator, and G_v is the first-order high pass filter used for active damping [4].

The corresponding control block diagram is shown in Fig. 6. To perform the passivity-based stability analysis, the closed output admittance Y_{inv} of the L-inverter seen from the capacitor must be first derived. Using the similar method in [3], the control loop in the sideband frequency domain can be treated as an additional path which is paralleled with $G_1(s)$ in the perturbation frequency domain. According to Fig. 6, the transfer function of this additional path can be given by:

$$G_{add}(s) = \frac{G_2(s)\cdot G_2(\tilde{s})}{G_1(\tilde{s})}\cdot\frac{T_{eq}(\tilde{s})}{1-T_{eq}(\tilde{s})} \tag{9}$$

where $T_{eq}(\tilde{s})$ is the equivalent loop gain in the sideband frequency domain which can be expressed by:

$$T_{eq}(\tilde{s}) = \frac{G_1(\tilde{s})G_d(\tilde{s})\left[sL_2\cdot G_v(\tilde{s}) - (\tilde{s}^2L_2C+1)\cdot G_i(\tilde{s})\right]}{\tilde{s}^3L_1L_2C + \tilde{s}\left(L_1+L_2\right)} \tag{10}$$

Therefore, considering the dynamics in sideband frequency

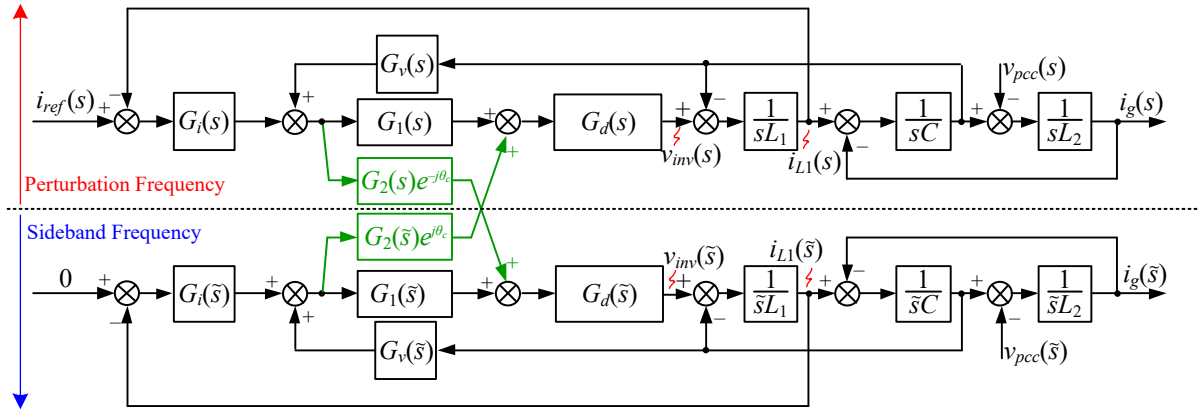

Fig. 6 Control block diagram of the three-phase grid-connected inverter

domain, the accurate transfer function of the digital SPWM modulator in the perturbation frequency domains can be derived as:

$$G_{1multi}(s) = G_1(s) + G_{add}(s) \tag{11}$$

So the accurate closed-loop admittance of the L-filtered inverter seen from the capacitor can also be derived as:

$$Y_{inv\_multi}(s) = \frac{1 - G_v(s)G_{1multi}(s)G_d(s)}{sL_1 + G_i(s)G_{1multi}(s)G_d(s)} \tag{12}$$

Meanwhile, the equivalent admittance of the rest passive components C and L_2 can be derived as:

$$Y_{eq}(s) = sC + \frac{1}{sL_2} \tag{13}$$

According to the passivity theory, the inverter is stable when the real part of the closed-loop admittance Y_{inv} is positive at all the frequencies where it is possible to intersect with the admittance of the rest passive components Y_{eq}. In other words, the phase of Y_{inv} should be limited between −90° and 90° at all the possible intersection frequencies.

IV. Experimental Verification

In order to exam the sideband effect on the inverter control, down-scaled three phase inverter is built, and parameters of inverters are shown in Tab. I. The resonance frequency of the LCL filter is 2.6kHz, which is close the half of the switching frequency.

Figs. 7 presents Bode diagrams of the admittance of L-inverter Y_{inv} and the rest passive components Y_{eq} in the perturbation domain. Fig.8 presents the zoom-in view of the two admittances around the intersection frequencies. As seen, the passivity of the L-inverter is influenced by the magnitude of the grid voltage when considering the sideband effect of the digital SPWM modulator. As seen, the system is stable when grid voltage is 90V and a resonance is expected when grid voltage is increased to 140V. The resonance should be around −3.1kHz and 2.9kHz.

Figs. 9 and 10 give the steady-state and dynamic

TABLE I

PARAMETERS OF GRID CONNECTED INVERTER

	Parameter	Values
V_{in}	Input dc-link voltage	400 V
V_g	Phase grid voltage, RMS	140 V
f_0	Fundamental frequency	50 Hz
f_{sw}	Switching frequency	6 kHz
f_s	Sampling frequency	12 kHz
L_f	Inverter-side inductor	1500μH
C_g	Grid capacitor	5μF
L_g	Grid inductor	1500μH

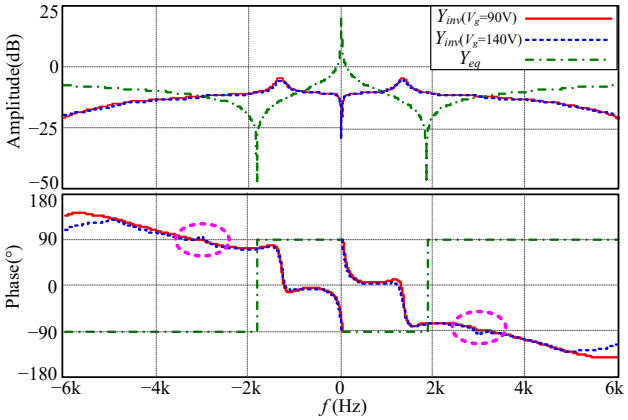

Fig. 7 Bode diagram of Y_{inv} and Y_{eq}

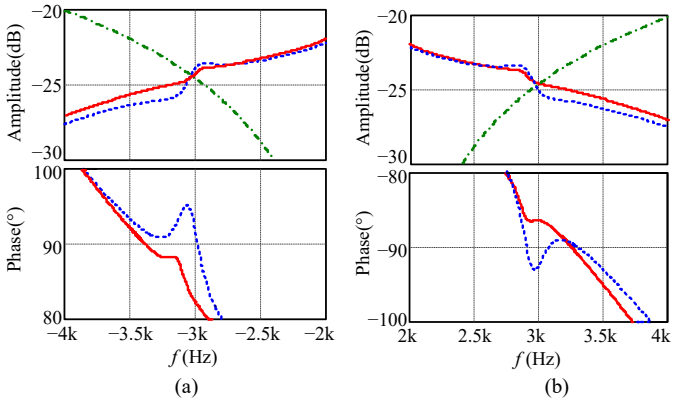

Fig. 8 Zoom-view of bode diagram of Y_{inv} and Y_{eq} around (a) negative intersection frequency (b) positive intersection frequency.

experimental results, respectively. As seen, the system is stable when grid voltage is 90V and an obvious resonance can be seen when the grid voltage becomes 140V. According to the FFT analysis, the resonance is mainly around 2.9 kHz and 3.1kHz. This resonance can not be prediected using the small signal averaged model which treats the grid voltage as an perturbation and can not change the system stability. So the experimental results confirm the effectiveness of the theoretical analysis.

V. Conclusion

To reduce the cost and volume of grid connected inverter, it is desirable to increase the resonance frequency of the LCL filter provided that the quality of the grid current is not compromised. Therefore, the sideband components generated by the digital SPWM modulation can impose a significant impact on the system stability. In this paper, the multifrequency model of the digital SPWM modulator is used to analyze the system stability instead of the common-used ZOH model. Using the passivity-based analysis method, the influence of grid voltage on the system stability can be successfully predicted, which provides a useful tool to study the stability of inverter in presence of large grid voltage disturbances. Experimental results from a down-scaled three-phase inverter confirm the effectiveness of stability analysis.

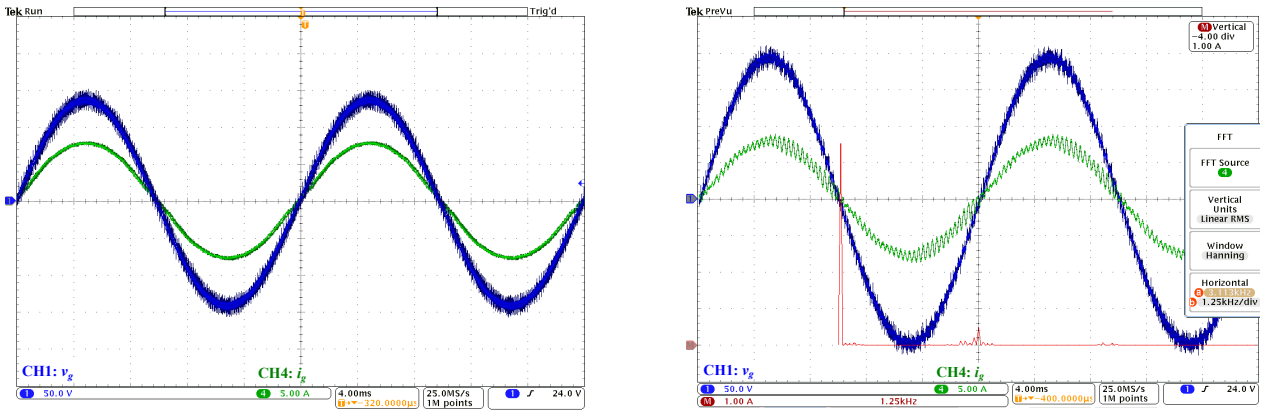

(a) (b)

Fig. 9 Steady-state waveforms when (a) V_g= 90V(rms) (b) V_g= 140V(rms)

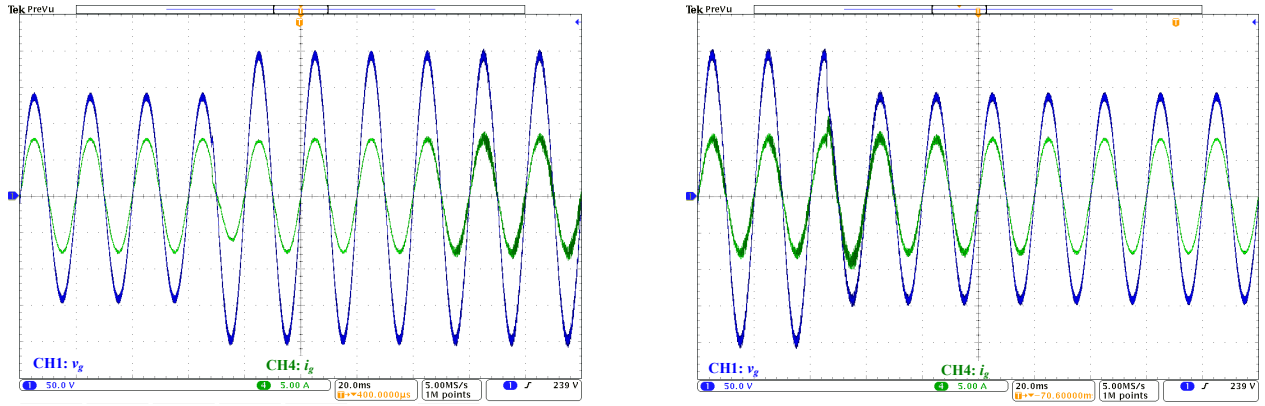

(a) (b)

Fig. 10 Dynamic waveforms when grid voltage is (a) step up from 90V(rms) to 140V(rms), (b) step down from 140V(rms) to 90V(rms).

REFERENCES

[1] F. Blaabjerg, R. Teodorescu, M. Liserre, and A. V. Timbus, "Overview of control and grid synchronization for distributed power generation systems," *IEEE Trans. Ind. Electron.*, vol. 53, no. 5, pp. 1398−1409, Oct., 2006.

[2] X. Wang; F. Blaabjerg, W. Wu, "Modeling and analysis of harmonic stability in an AC power-electronics-based power system," *IEEE Trans. Power Electron*., vol. 29, no. 12, pp. 6421-6432, Dec., 2014.

[3] J. Sun, "Impedance-based stability criterion for grid-connected inverters," *IEEE Trans. Power Electron.*, vol. 26, no. 11, pp. 3075–3078, Nov., 2011.

[4] L. Harnefors, A. G. Yepes, A. Vidal, and J. Doval-Gandoy, "Passivity-based controller design of grid-connected VSCs for prevention of electrical resonance instability," *IEEE Trans. Ind. Electron.*, vol. 62, no. 2, pp. 702−710, 2015.

[5] D. Yang, X. Ruan, and H. Wu, "Impedance shaping of the grid-connected inverter with LCL filter to improve its adaptability to the weak grid condition," *IEEE Trans. Power Electron*., vol. 29, no. 11, pp. 5795–5805, Nov., 2014.

[6] L. Harnefors, M. Bongiorno, and S. Lundberg, "Input-admittance calculation and shaping for controlled voltage-source converters," *IEEE Trans. Ind. Electron.*, vol. 54, no. 6, pp. 3323–3334, Dec., 2007.

[7] J. Agorreta, M. Borrega, J. Lopez, and L. Marroyo, "Modeling and control of N-paralleled grid-connected inverters with LCL filters coupled due to grid impedance in PV plants, " *IEEE Trans. Power Electron*., vol. 26, no. 3, pp. 770-1194, Mar., 2011.

[8] Y. Tang, W. Yao, P. Loh, and F. Blaabjerg, "Design of LCL-filters with LCL resonance frequencies beyond the Nyquist frequency for grid-connected converters," *IEEE J. Emerg. Sel. Topics Power Electron*., vol. 4, no. 1, pp. 3–14, Mar., 2015.

[9] W. Wu, Y. He, and F. Blaabjerg, "An LLCL power filter for single-phase grid-tied inverter," *IEEE Trans. Power Electron*., vol. 27, no. 2, pp. 782–789, Jan., 2012.

[10] Y. Qiu, M. Xu, K. Yao, J. Sun, F. C. Lee, "Multifrequency small-signal model for buck and multiphase buck converters," *IEEE Trans. Power Electron.*, vol. 21, no. 5, pp. 1185−1192, 2006.

[11] X. Yue, Z. Fang, S. Yang, Y. Pei, and H. Yi, "A Matrix-Based Multi-Frequency Output Impedance Model for Beat Frequency Oscillation Analysis in Distributed Power Systems, " ," *IEEE J. Emerg. Sel. Topics Power Electron.*, Vol. 4, no. 1, pp. 80-92, Mar.2016.

[12] L. Harnefors, R. Finger, X. Wang, H. Bai, and F. Blaabjerg, "VSC input-admittance modeling and analysis above the Nyquist frequency for passivity-based stability assessment," *IEEE Trans. Ind. Electron.,* in press.

[13] D. Holmes and T. Lipo, *Pulse Width Modulation for Power Converters (Principles and Practice)* (IEEE Press Series on Power Engineering). Hoboken, NJ, USA: Wiley 2003.

[14] J. Sun, Z. Bing, and K. J. Karimi, "Input impedance modeling of multipulse rectifiers by harmonic linearization," *IEEE Trans. Power Electron*., vol. 24, no. 12, pp. 2812–2820, Dec., 2009.

[15] H. Mouton, B. McGrath, D. G. Holmes, R. H. Wilkinson, "One-dimensional spectral analysis of complex PWM waveforms using superposition," *IEEE Trans. Power Electron*., vol. 29, no. 12, pp. 6762-6778, 2014.